crystals

MDPI

Article

A-Site Ion Doping in $Cs_2AgBiBr_6$ Double Perovskite Films for Improved Optical and Photodetector Performance

Yuejia Wu, Yanpeng Meng, Qirun Hu, Songchao Shen, Chengxi Zhang, Ang Bian * and Jun Dai

School of Science, Jiangsu University of Science and Technology, Zhenjiang 212100, China
* Correspondence: angbian@just.edu.cn

Abstract: Perovskite materials, as emerging semiconductors, have attracted significant attention for their exceptional optoelectronic properties, tunable bandgaps, ease of fabrication, and cost-effectiveness, making them promising candidates for next-generation optoelectronic devices. The all-inorganic perovskite $Cs_2AgBiBr_6$ distinguishes itself from other perovskite materials due to its remarkable optical absorption and emission properties, excellent stability, prolonged carrier recombination lifetime, and nontoxic characteristics. However, a deeper understanding of its unique luminescent properties and a further optimization of its structure and performance are still necessary. This study systematically investigates the optimization of $Cs_2AgBiBr_6$ double perovskite films through A-site Na^+ doping. At an optimal Na^+ doping concentration of 3.5% ($Na_{0.07}Cs_{1.93}AgBiBr_6$), the film shows 1.4 times and 2.7 times enhancement in light absorption and photoluminescence intensity, compared to the undoped film. Low-temperature spectroscopy measurements indicate that $Na_{0.07}Cs_{1.93}AgBiBr_6$ exhibits higher exciton binding energy and phonon energy. Based on $Na_{0.07}Cs_{1.93}AgBiBr_6$, the photodetectors demonstrate significant performance improvements, with a high photocurrent response of 10^{-2} A, a photo-to-dark current ratio (*PDCR*) of 7.57×10^4, a responsivity (*R*) of 16.23 A/W, a detectivity (*D**) of 2.92×10^{12} Jones, a linear dynamic range (*LDR*) of 98.75 dB, and a fast response time of 943 ms. This work provides a promising strategy for optimizing all-inorganic perovskite materials through doping and offers guidance for enhancing high-performance photodetectors.

Keywords: double perovskite; alkali ion doping; $Cs_2AgBiBr_6$; photoluminescence; photodetectors

check for updates

Citation: Wu, Y.; Meng, Y.; Hu, Q.; Shen, S.; Zhang, C.; Bian, A.; Dai, J. A-Site Ion Doping in $Cs_2AgBiBr_6$ Double Perovskite Films for Improved Optical and Photodetector Performance. *Crystals* **2024**, *14*, 1068. https://doi.org/10.3390/cryst14121068

Academic Editor: Sawanta Mali

Received: 16 November 2024
Revised: 8 December 2024
Accepted: 9 December 2024
Published: 12 December 2024

Copyright: © 2024 by the authors. Licensee MDPI, Basel, Switzerland. This article is an open access article distributed under the terms and conditions of the Creative Commons Attribution (CC BY) license (https://creativecommons.org/licenses/by/4.0/).

1. Introduction

Lead-based perovskite materials have attracted tremendous attention in high-performance optoelectronic applications due to their high light absorption coefficient, long carrier diffusion lengths, tunable direct bandgap, and high defect tolerance [1–4]. Organic–inorganic hybrid lead-based perovskites have demonstrated promising potential and notable advancements in the field of solar cells [5–7], as well as important breakthroughs in various optoelectronic applications, including photodetectors (PDs), X-ray imaging, and light-emitting diodes (LEDs) [8–11]. Despite their excellent performance, the lead-based perovskites are still facing the challenges of long-term stability arising from the degradation of organic components and the environmental toxicity associated with lead. To overcome the issues of instability and lead toxicity, significant efforts have been devoted to the development of lead-free perovskite materials.

As a lead-free double perovskite material, $Cs_2AgBiBr_6$ has emerged as a potential candidate for optoelectronic devices due to its unique luminescent properties, environmental friendliness, long carrier recombination lifetime, and excellent stability [12–14]. Karunadasa et al. reported the inherent high defect tolerance of $Cs_2AgBiBr_6$ in 2016 [15]. Bein et al. introduced $Cs_2AgBiBr_6$ thin films into solar cells as an active layer achieving a low power conversion efficiency of 2.5%, which marked a significant step towards practical applications [16]. Subsequently, innovative applications of $Cs_2AgBiBr_6$ have been reported

in the high-performance X-ray detectors [17], photodetectors [18], and photocatalytic systems [19]. However, $Cs_2AgBiBr_6$ double perovskite materials still need optimization in their optical or electronic properties, with progress being made through various approaches [20]. For example, the incorporation of 1-butyl-2,3-dimethylimidazolium chloride ionic liquid into the precursor [21], or the improvement of vacuum thermal evaporation and annealing processes [22], has been shown to significantly enhance the quality of $Cs_2AgBiBr_6$ films.

In addition to improvements in preparation methods, ion doping strategies have proven to be effective tools for tuning the performance and applications of semiconductor materials. Doping with iron (Fe) and copper (Cu) has been shown to enhance the photoluminescent properties of double perovskites [23,24]. Recently, alkali metal ion doping has been found to significantly improve the crystal quality and optoelectronic performance of perovskite films. For example, Wang et al. enhanced the photoluminescence quantum yield of $Cs_2AgBiBr_6$ by incorporating Na^+ ions into the Ag sites [25]. Ding et al. achieved highly sensitive $Cs_2AgBiBr_6$ double perovskite photodetectors through co-doping with Na^+/Ce^{3+} [26]. Chen et al. demonstrated that substituting Ag^+ with Rb^+ effectively tunes the electronic structure of $Cs_2AgBiBr_6$, thereby enhancing its photocatalytic CO_2 reduction performance [27]. Additionally, theoretical and experimental studies have investigated Ru doping in $Cs_2AgBiBr_6$ [28,29]. However, research on A-site doping in double perovskites remains relatively limited [30,31], particularly concerning the study of optical properties and a deeper understanding of the fundamental aspects of detection performance. These doping strategies still require further optimization to fully realize their potential in enhancing the optical and electronic properties of the material.

This study investigates the effect of A-site Na ion doping on the properties of all-inorganic $Cs_2AgBiBr_6$ perovskite thin films and explores its potential for enhancing photodetection capabilities. The results show that Na^+ doping not only refines the crystal structure and morphology of $Cs_2AgBiBr_6$, but also optimizes its optoelectronic properties by modulating its electronic characteristics and reducing nonradiative recombination losses. Consequently, Na^+-doped $Cs_2AgBiBr_6$ photodetectors exhibit significantly improved photoresponse characteristics. These findings suggest that sodium doping is a promising strategy for enhancing the performance of $Cs_2AgBiBr_6$-based photodetectors and other optoelectronic applications.

2. Experimental Methods

The precursor material $Cs_2AgBiBr_6$ is synthesized by dissolving CsBr, AgBr, and $BiBr_3$ in a 2:1:1 molar ratio in 1 mL of dimethyl sulfoxide (DMSO). The precursor mixture is stirred for 3–4 h at 80 °C under a nitrogen atmosphere within a glovebox to ensure complete dissolution, resulting in a homogeneous precursor solution. For doping, a portion of the $Cs_2AgBiBr_6$ precursor solution is mixed with sodium bromide (NaBr) powder as the dopant. The doping concentrations are 2.5%, 3.5%, and 5% by molar ratio of NaBr to the total halide content. This leads to the formation of the doped materials $Na_{0.05}Cs_{1.95}AgBiBr_6$, $Na_{0.07}Cs_{1.93}AgBiBr_6$, and $Na_{0.1}Cs_{1.9}AgBiBr_6$, respectively. The quartz glass substrates are then sequentially cleaned via ultrasonic treatment in distilled water, deionized water, acetone, and ethanol for 15 min each, followed by drying and UV–ozone treatment for another 15 min. Subsequently, the preheated precursor solution at 80 °C is spin-coated onto the cleaned quartz substrate at 3000 rpm for 50 s to form the thin film. To induce crystallization, the coated substrate is annealed on a hot plate at 285 °C for 5 min, promoting the formation of its crystalline structure. The preparation of the detector device adopts a planar structure configuration, with fluorine-doped tin oxide (FTO) as the transparent conductive substrate and Ag as the top electrode. After spin-coating the perovskite film on the substrate, patterned silver electrodes are fabricated on the film surface using a mask and thermal evaporation.

The structure and morphology of the films were characterized using well-established commercial techniques, including X-ray diffraction (XRD) (SmartLab, Rigaku, Akishima, Japan), scanning electron microscopy (SEM) (Quanta FEG 250, FEI Company, Beaverton,

OR, USA), and X-ray photoelectron spectroscopy (XPS) (D8 Advance, Bruker Corporation, Billerica, MA, USA). The ultraviolet–visible absorption spectra were obtained using a U-4100 ultraviolet–visible (UV–vis) spectrophotometer (HITACHI, Tokyo, Japan). Photoluminescence (PL) at room temperature was excited with a 325 nm laser and measured using a custom-built spectrometer (Acton Spectra Pro 2300, Princeton Instruments, Trenton, NJ, USA). Ultralow temperature photoluminescence spectra were excited with a 405 nm laser and recorded using an Optistat Dry system (Oxford Instruments, Concord, MA, USA) with a temperature range of 5–300 K. The response performance of the prepared photodiode was tested by using the Keithley 4200-SCS semiconductor parameter instrument (Tektronix, Beaverton, OR, USA). The UV lamp that can emit 405 nm wavelength was used as the light source, and the optical power of the irradiated light was regulated by adjusting the distance between the sample and the light source.

3. Results and Discussion

The optical image of the Na^+-doped double perovskite photodetector on FTO was prepared in the experiment shown in Figure 1a. The silver electrode, after thermal deposition, exhibits a smooth and uniform appearance, forming good contact with the perovskite layer. Figure 1b presents the optical image at 100× magnification, showing a uniform surface and a well-ordered perovskite thin film.

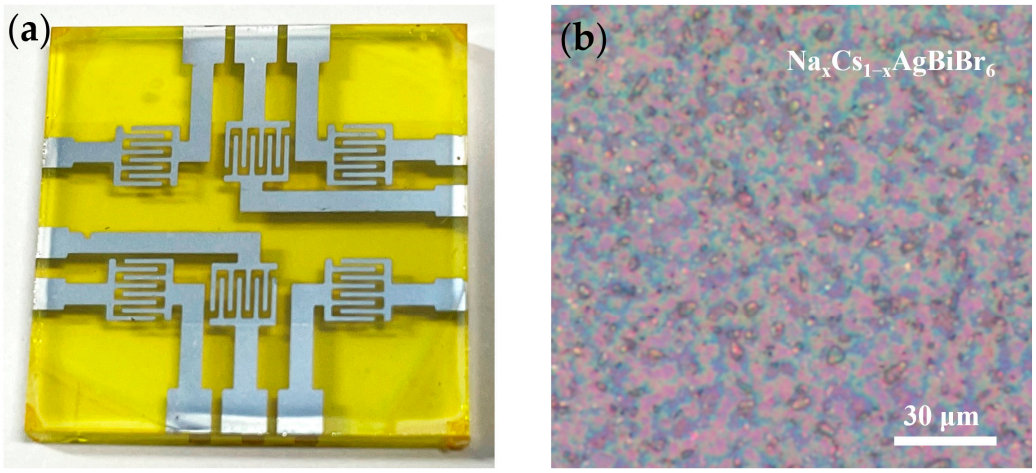


Figure 1. (**a**) Photodetector based on $Na_xCs_{2-x}AgBiBr_6$. (**b**) Optical microscope image of $Na_xCs_{2-x}AgBiBr_6$ thin film.

The SEM images of $Na_xCs_{2-x}AgBiBr_6$ thin films with different doping levels are shown in Figure 2. In comparison to undoped $Cs_2AgBiBr_6$, the Na^+-doped perovskite films exhibit increased crystal sizes and a reduction in pinhole density. As the Na^+ doping concentration increases, the average grain size first increases and then decreases, while the number of pinholes first decreases and then significantly increases. SEM analysis indicates that at a 3.5% Na^+ doping level, $Na_{0.07}Cs_{1.93}AgBiBr_6$ films exhibit the best surface morphology, showing good morphology and high compactness with no small grains at the grain boundaries or significant pinholes. Using Nano Measurer software (version 1.2), the grain size of $Na_{0.07}Cs_{1.93}AgBiBr_6$ is measured to be 320 nm, which is larger than that of the other samples: $Cs_2AgBiBr_6$ (240 nm), $Na_{0.05}Cs_{1.95}AgBiBr_6$ (286 nm), and $Na_{0.1}Cs_{1.9}AgBiBr_6$ (318 nm). The increase in grain size can be attributed to Na^+ providing nucleation sites for film growth and regulating the crystallization rate, effectively reducing the number of grain boundaries, facilitating carrier migration, and enhancing optoelectronic performance [32].

At the same time, the white spots observed on the surface of the Na^+-doped $Cs_2AgBiBr_6$ double perovskite in Figure 2 may be due to the local aggregation of Na^+ ions or minor surface defects generated during the doping process. During Na^+ doping, certain regions may exhibit slightly higher Na^+ concentrations, forming aggregates that appear as bright spots

in the SEM images. These spots may also originate from surface roughness or small defects formed during the film deposition process, which are common characteristics associated with ion doping. Furthermore, the observed variation in gray shading is not caused by phase separation but results from differences in surface morphology and grain size, which affect electron scattering during SEM imaging [31].

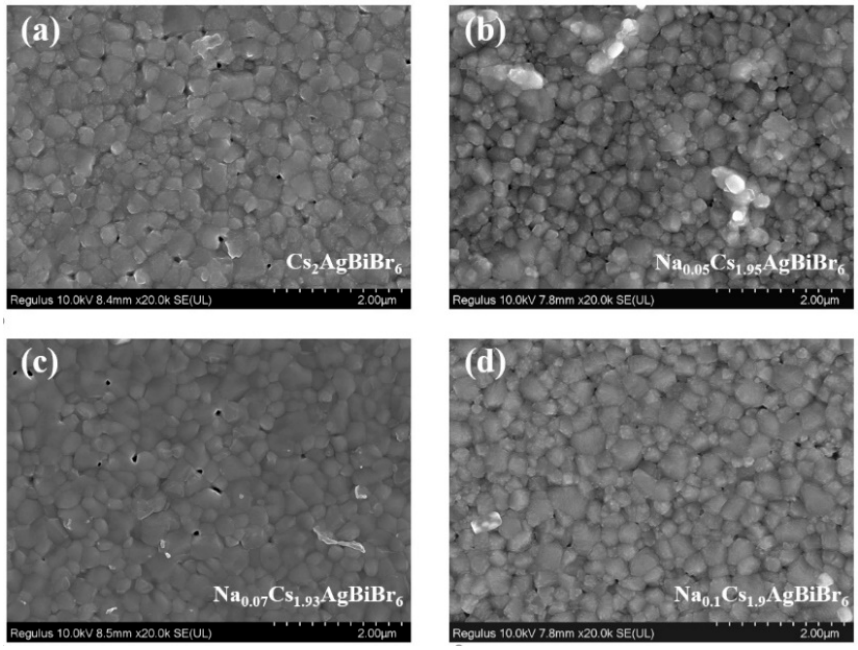


Figure 2. SEM morphology of (**a**) undoped $Cs_2AgBiBr_6$, (**b**) $Na_{0.05}Cs_{1.95}AgBiBr_6$, (**c**) $Na_{0.07}Cs_{1.93}AgBiBr_6$, and (**d**) $Na_{0.1}Cs_{1.9}AgBiBr_6$ films on the Quartz glass.

To assess the impact of different doping conditions on the crystalline quality, the XRD patterns of $Na_xCs_{2-x}AgBiBr_6$ thin films were analyzed, as shown in Figure 3. Prior to doping, the XRD diffraction peaks of $Cs_2AgBiBr_6$ were observed at 14.1°, 16.2°, 22.7°, 26.9°, 27.8°, 32.2°, 36.1°, 39.6°, 46.0°, and 48.8°, corresponding to the (111), (002), (022), (113), (222), (004), (024), (224), (044), and (244) crystal planes of the cubic phase of $Cs_2AgBiBr_6$, respectively [33]. After doping, no additional peaks appeared in the XRD patterns, indicating that the Na^+ incorporation did not alter the crystal structure, and all samples maintained the double perovskite Fm-3m cubic space group. Notably, the intensities of the (002) and (004) peaks at 22.7° and 32.2° increased, which can show that Na^+ doping improves the crystallinity of the perovskite film. When the Na^+ doping concentration is 3.5%, the corresponding diffraction peak intensity is the highest and the crystallinity is the best. This suggests that Na^+ doping enhances the preferred orientation of these crystal planes during the crystallization process of the $Cs_2AgBiBr_6$ films. Additionally, a detailed refinement of the XRD data was performed. The refined XRD patterns are presented in Figure S1, where the red curve represents the original data, the blue curve shows the difference, the black curve indicates the fitted data, and the green markers denote the characteristic peaks of the structure. The refinement parameters, R and X, are within acceptable limits ($R < 10$, $X < 3$), confirming the reliability of the data. The comparison of refinement parameters in Tables S1–S4 shows that the positions of Na^+ ions coincide with those of Cs^+ ions, confirming that Na^+ ions occupy the A-site and successfully substitute the Cs^+ ions. This substitution may result in a slight shift in the XRD peak positions, further confirming that Na^+ has successfully incorporated into the $Cs_2AgBiBr_6$ structure, thereby improving the crystal quality and enhancing the optoelectronic performance.

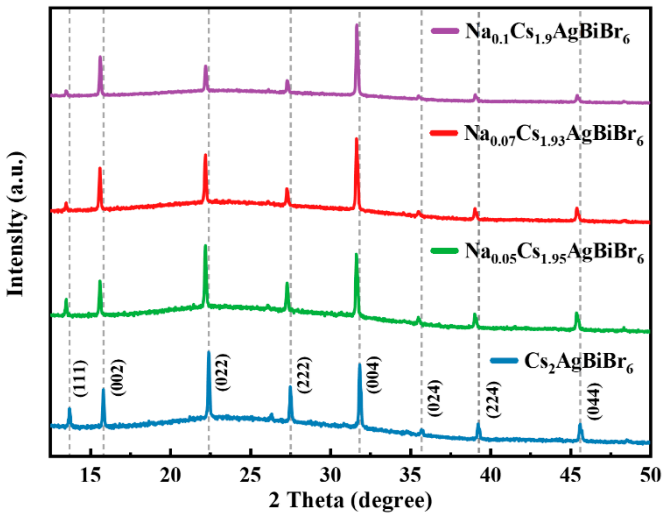


Figure 3. XRD pattern of undoped $Cs_2AgBiBr_6$ and $Na_xCs_{2-x}AgBiBr_6$ perovskite film.

For further analysis of the samples, X-ray photoelectron spectroscopy (XPS) was employed to analyze the electronic interactions in $Cs_2AgBiBr_6$ films before and after Na^+ doping as shown in Figure 4a. Overall, both XPS spectra show the characteristic peaks of $Cs_2AgBiBr_6$. However, in the high-resolution XPS spectrum shown in Figure 4b, the Na 1s peak is only observed in the doped sample. The binding energy of Na 1s is 1072 eV, indicating that Na^+ has been successfully incorporated into $Cs_2AgBiBr_6$. In Figure 4c, by comparing the Cs 3d core-level spectra, a notable shift of the XPS peak towards higher binding energy was observed in the $Na_{0.07}Cs_{1.93}AgBiBr_6$ films, indicating an increase in binding energy. This shift is attributed to the substitution of Cs^+ by Na^+, with the difference in ionic radii affecting the ionic attraction [31]. This substitution reduces anti-site defects in the lattice, thereby decreasing the surface defect state density. At the same time, there was little change in the binding energy of the Ag 3d peaks, suggesting that, unlike previous studies, Na^+ did not replace Ag^+ in this work. This doping could break the inversion symmetry-induced parity-forbidden transitions, altering the wave function symmetry of self-trapped excitons at Ag atoms, thereby promoting radiative recombination and reducing surface defects in the film [25]. The effects of doping are also reflected in the peak shifts of the Bi 4f and Br 3d spectra, indicating a reduction in the oxidation states of Br and Bi elements, possibly due to a partial overlap between the Na 1s and Cs 3d peaks. These results confirm that Na^+ was successfully doped into $Cs_2AgBiBr_6$ and partially replaced Cs^+, indicating that the synthesized material is not a ternary compound.

In addition, the valence band maximum of $Cs_2AgBiBr_6$ is primarily contributed by the Br-4p and Ag-4d orbitals, while the conduction band minimum is mainly influenced by the Bi-6p and Br-4p orbitals [34]. As the Na^+ doping level increases, the Ag electronic states significantly deplete, weakening the interaction between the Br-4p and Ag-4d states. This reduction in interaction leads to a lowering of the valence band maximum, resulting in a broader indirect bandgap at higher Na^+ doping concentrations. Therefore, this phenomenon was further investigated through absorption and photoluminescence spectroscopy analysis.

Figure 5a shows the ultraviolet–visible (UV–vis) absorption spectra of undoped and Na^+-doped $Cs_2AgBiBr_6$ films. Both $Cs_2AgBiBr_6$ and $Na_xCs_{2-x}AgBiBr_6$ exhibit an absorption tail at longer wavelengths near 500 nm, indicating the presence of an indirect bandgap, consistent with previous research [35]. The main absorption peak of both undoped and doped $Cs_2AgBiBr_6$ is located around 440 nm, corresponding to band-edge exciton absorption, with no shift observed. In addition, a notable absorption peak around 350 nm is observed, attributed to direct bandgap absorption [36]. As the doping concentration increases, the light absorption intensity improves, with a notable enhancement of approximately 1.4 times

observed when the doping level reaches 3.5%. Therefore, a 405 nm laser can be effectively used to excite the band-edge excitons of $Cs_2AgBiBr_6$, resulting in PL emission.

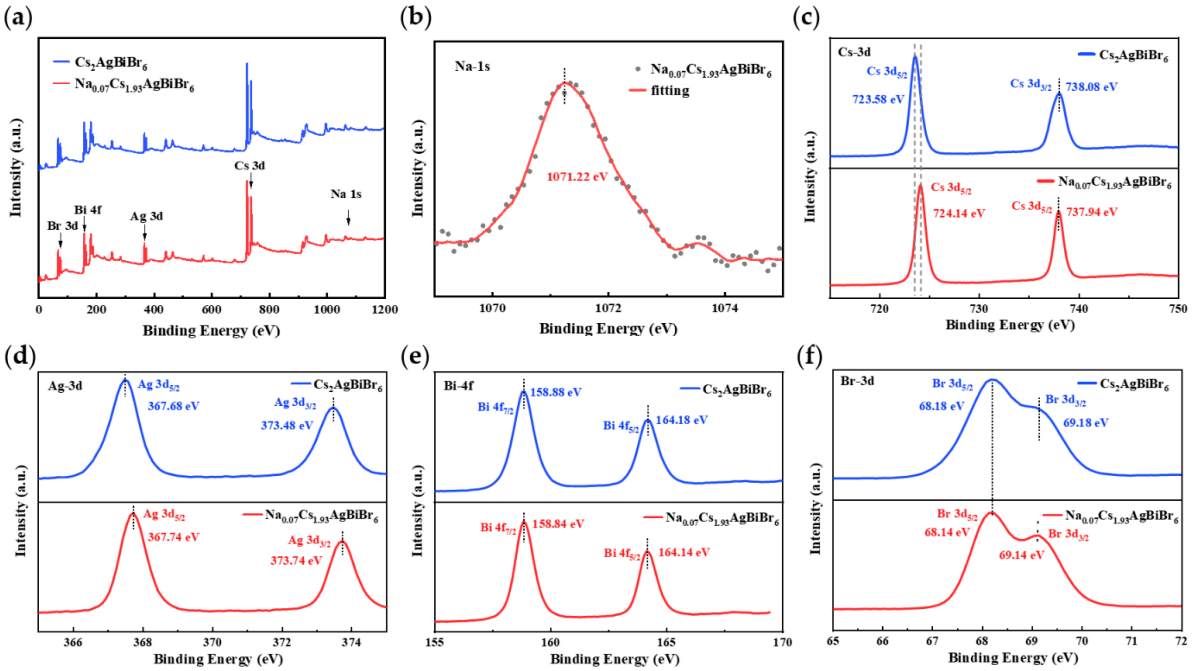


Figure 4. (**a**) Comparison of XPS spectra of $Cs_2AgBiBr_6$ and $Na_{0.07}Cs_{1.93}AgBiBr_6$ film; (**b**–**f**) high-resolution XPS spectra of core levels for Na 1s, Cs 3d, Ag 3d, Bi 4f, and Br 3d, respectively.

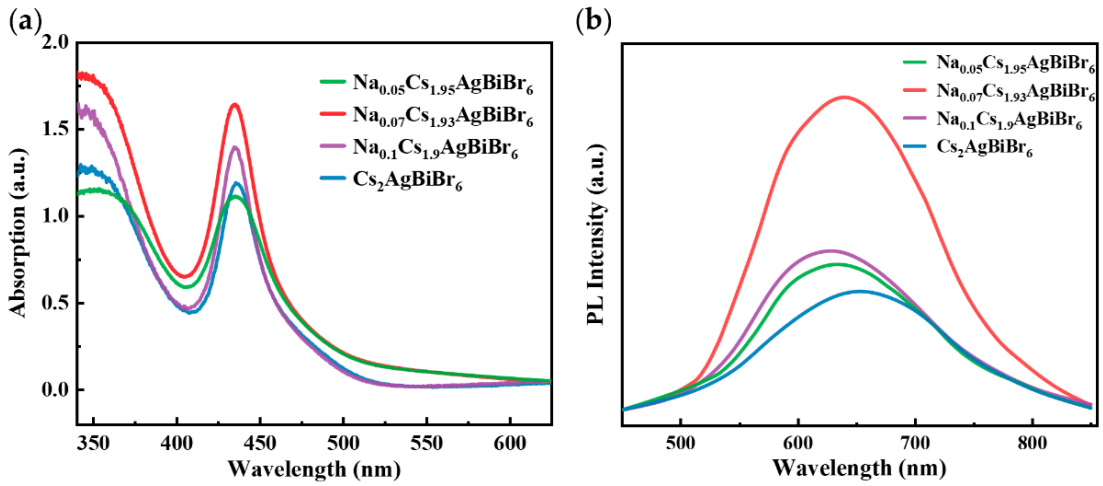


Figure 5. (**a**) UV–vis absorption spectrum and (**b**) PL spectrum under 325 nm excitation of undoped $Cs_2AgBiBr_6$ and $Na_xCs_{2-x}AgBiBr_6$ film at room temperature.

The PL spectra of undoped and Na-doped $Cs_2AgBiBr_6$ double perovskite films is shown in Figure 5b. Due to the indirect bandgap nature of the material, no obvious peak is observed near the exciton absorption peak. However, the $Cs_2AgBiBr_6$ films exhibit a broad emission peak centered at approximately 650 nm. In indirect bandgap semiconductors, nonradiative channels dominate the process of photogenerated carriers. Nevertheless, weak PL is generally still observed due to intrinsic recombination. The large shift in the emission peak, however, is due to the recombination process associated with self-trapped excitons (STEs) in the energy band [37].

After doping with Na^+ ions, both the intensity of the broad emission peak and the position of the PL peak shift with increasing doping concentration, indicating that Na^+

doping can alter the optical bandgap structure of the double perovskite [32]. At a Na^+ doping concentration of $Na_{0.07}Cs_{1.93}AgBiBr_6$, the film exhibits a significant blue shift in the emission, with the broad emission peak centered at 600 nm, and the emission intensity reaches its maximum, 2.7 times higher than that of the undoped $Cs_2AgBiBr_6$, as shown by the red curve in Figure 5b. This is likely because the introduction of sodium ions enhances electron–phonon interactions [38], thereby promoting the formation of more STE states, which increases the PL intensity [23,39].

The optical properties of $Cs_2AgBiBr_6$ films were further investigated through temperature-dependent PL spectra analysis in the temperature range of 10–210 K, as shown in the two-dimensional color maps in Figure 6. At low temperatures, both doped and undoped samples exhibit a noticeable increase in emission intensity. Notably, the $Na_{0.07}Cs_{1.93}AgBiBr_6$ film shows significantly higher PL intensity at low temperatures compared to $Cs_2AgBiBr_6$ films, without a shift in the peak position, which are at 622 nm and 600 nm, respectively. As the temperature increases, the PL intensity gradually decreases, which is attributed to the enhanced electron–phonon interaction [40]. This increase in interaction leads to a higher probability of nonradiative recombination, thereby reducing the PL intensity [34]. It is worth noting that the slight difference in peak positions between the room temperature and variable temperature PL spectra is due to the use of different excitation sources and optical setups. Nevertheless, both spectra accurately reflect the luminescent properties before and after doping, maintaining consistent trends.

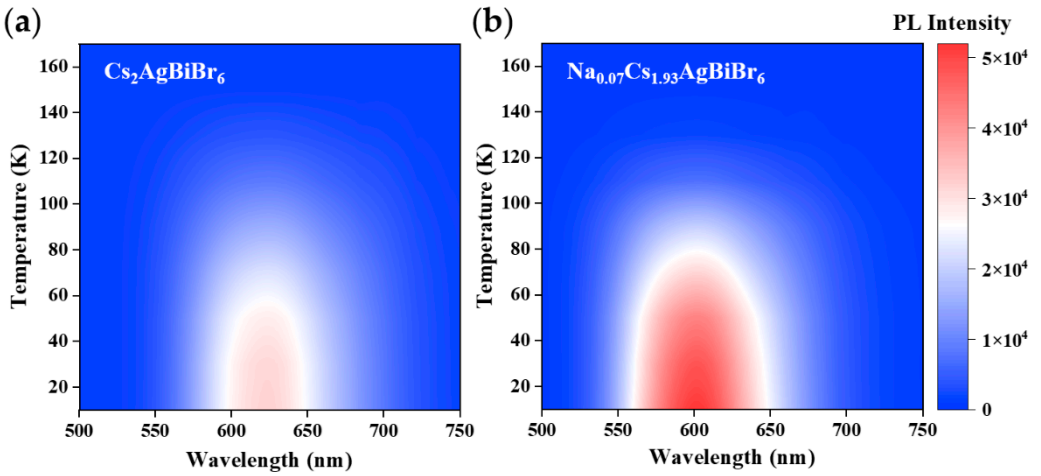


Figure 6. (**a**) $Cs_2AgBiBr_6$ and (**b**) $Na_{0.07}Cs_{1.93}AgBiBr_6$ temperature-dependent photoluminescence spectral contours under 405 nm excitation.

To extract the exciton binding energy, the relationship between intensity and temperature can be fitted by the Arrhenius equation:

$$I(T) = \frac{I_0}{1 + Ae^{\frac{E_B}{k_B T}}} \quad (1)$$

where I_0 are PL integral intensities at temperatures of 0 K. A is the fitting constant, k_B is the Boltzmann constant, and E_B is the exciton binding energy. According to the fitting results in Figure 7a, the fitting values of exciton binding energy of $Cs_2AgBiBr_6$ and $Na_{0.07}Cs_{1.93}AgBiBr_6$ thin films are 37.75 meV and 38.83 meV, respectively. The larger exciton binding energy of $Na_{0.07}Cs_{1.93}AgBiBr_6$ promotes radiative recombination, leading to a stronger emission.

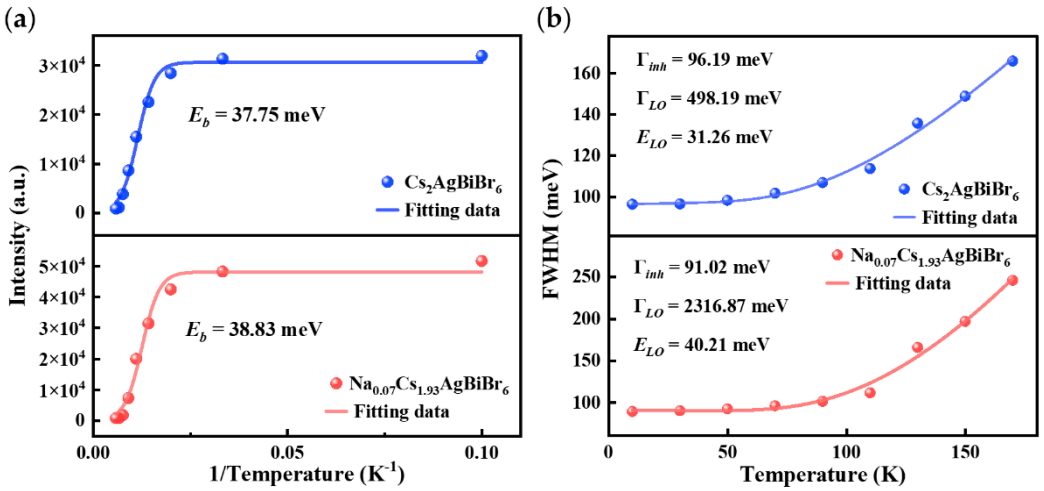


Figure 7. Fitting of (**a**) peak intensity and (**b**) FWHM from temperature-dependent PL spectra of $Cs_2AgBiBr_6$ and $Na_{0.07}Cs_{1.93}AgBiBr_6$ films.

The variation of the full width at half maximum (FWHM) of the PL spectra with temperature is commonly used to study phonon scattering in perovskite materials. Therefore, FWHM can be used to analyze the changes in exciton–phonon interactions before and after doping during carrier recombination. Figure 7b shows the variation trend of FWHM of $Cs_2AgBiBr_6$ and $Na_{0.07}Cs_{1.93}AgBiBr_6$ with temperature. Fitting using the independent Boson model, the relationship between temperature-dependent FWHM temperatures can be fitted using the Boson formula [41]:

$$\Gamma(T) = \Gamma_{inh} + \sigma T + \frac{\Gamma_{LO}}{\exp(\frac{E_{LO}}{k_B T}) - 1} \quad (2)$$

where Γ_{inh} is the nonuniform bandwidth of the FWHM caused by the nonuniformity of the sample, such as the size and shape of the quantum dot, and σ is the exciton–acoustic phonon coupling coefficient. Γ_{LO} is the exciton–longitudinal mode optical phonon (LO) coupling coefficient. E_{LO} is the longitudinal mode optical phonon energy. The parameters obtained by fitting are shown in Table 1.

Table 1. Comparison of fitting parameters for $Cs_2AgBiBr_6$ and $Na_{0.07}Cs_{1.93}AgBiBr_6$.

	E_B (meV)	Γ_{inh} (meV)	σ (μeV/K)	Γ_{LO} (meV)	E_{LO} (μeV)
$Cs_2AgBiBr_6$	37.75	96.19	23.32	511.89	31.26
$Na_{0.07}Cs_{1.93}AgBiBr_6$	38.83	91.02	12.32	2316.39	40.21

The FWHM of the PL spectra of both films broadens with increasing temperature, which is the result of a combination of nonuniform broadening due to molecular collisions and uniform broadening due to photon–phonon interactions. From the fitting results of Figure 7b, $Cs_2AgBiBr_6$ has a smaller value of E_{LO} (31.26 μeV), which indicates that more phonons are produced, and these phonons become nonradiative recombination centers during exciton recombination. Meanwhile, $Na_{0.07}Cs_{1.93}AgBiBr_6$ exhibits a higher E_{LO} value (40.21 μeV), indicating that there is a strong exciton–phonon interaction and a weak nonradiative transition during exciton recombination, which further proves that the luminous efficiency of $Na_{0.07}Cs_{1.93}AgBiBr_6$ is higher than that of $Cs_2AgBiBr_6$.

To evaluate the impact of Na^+ doping on the optoelectronic properties of $Cs_2AgBiBr_6$ films and explore their potential application in photodetection, the optimized $Na_{0.07}Cs_{1.93}AgBiBr_6$ film was used as the photoactive layer to fabricate a photodetector, with the undoped $Cs_2AgBiBr_6$ film serving as a reference for comparison. The $Cs_2AgBiBr_6$ film was fabricated

using a one-step solution process with FTO as the substrate. Silver films were used as contact electrodes, resulting in a conductive substrate–semiconductor-metal structure.

Figure 8 details a comparison of the performance between photodetectors $Cs_2AgBiBr_6$ and $Na_{0.07}Cs_{1.93}AgBiBr_6$. In Figure 8a, the current–voltage (I-V) curve of the n-i-p structure is depicted under 405 nm illumination at an intensity of 5 W/m^2 and a bias voltage varying between ±5 V. The data indicate that both the dark current and photocurrent are significantly enhanced in the devices with Na^+ doping, suggesting a relatively low Schottky barrier at the $Ag/Cs_2AgBiBr_6$ interface. A slight reduction in the external bias voltage effectively compensates for this barrier, facilitating the transport of photo-generated carriers from $Cs_2AgBiBr_6$ to the metal contact electrode, which in turn, substantially increases the photocurrent. Under a 5 V bias, the dark current of $Na_{0.07}Cs_{1.93}AgBiBr_6$. is enhanced by approximately four orders of magnitude compared to undoped films, indicating that doping effectively passivates film defects and extends the carrier diffusion length. Figure 8b illustrates the $Na_{0.07}Cs_{1.93}AgBiBr_6$ dynamic response (I-T) of the current under varying light power during switching illumination, measured at a constant bias voltage of 5 V. The incident light was applied for 20 s in each cycle. The results show that the device exhibits rapid cycling stability and repeatability, with the photocurrent significantly increasing as light irradiation power rises. Figure 8c demonstrates that the photocurrent of the $Cs_2AgBiBr_6$ film photodetector exhibits a linear relationship with light power from 20 mW to 50 mW, enabling accurate power-resolved photoelectric detection.

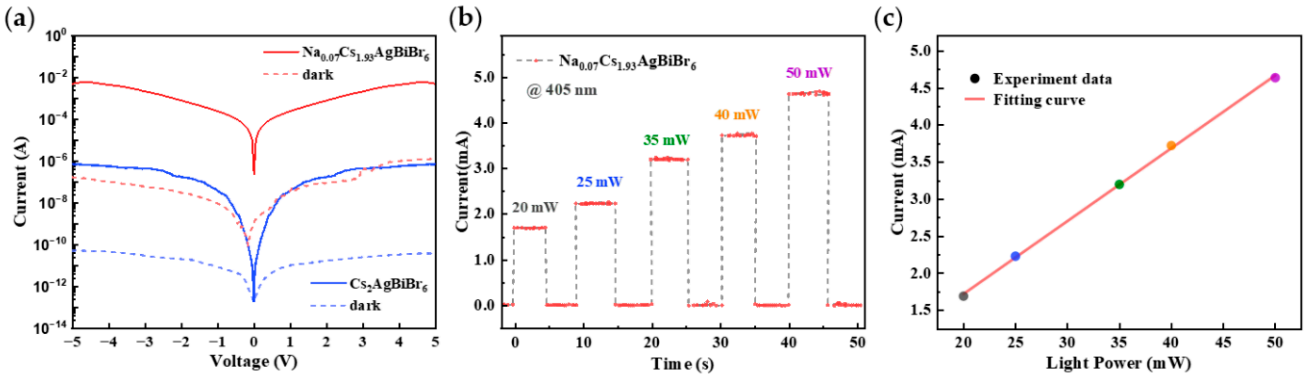


Figure 8. (**a**) Typical current–voltage (I-V) characteristics of undoped $Cs_2AgBiBr_6$ and $Na_{0.07}Cs_{1.93}AgBiBr_6$ films under both dark and 405 nm illuminated conditions. (**b**) The dynamic current–time response (I-T) curves of the $Na_{0.07}Cs_{1.93}AgBiBr_6$ device at a 5 V bias under 405 nm illumination with different power. (**c**) The linear fit of the relationship between peak current and light power.

Based on the evaluation of the detector performance, key optoelectronic parameters are primarily selected for comparison, including linear dynamic range (*LDR*), photocurrent-to-dark current ratio (*PDCR*), responsivity (*R*), and specific detectivity (*D**), with the following definitions:

The *LDR* reflects the linear relationship between photocurrent and light radiation intensity, defined as follows:

$$LDR = 20 \log \frac{I_p}{I_d} \quad (3)$$

where $I_{p\ p}$ is the photocurrent and I_d is the dark current. The *LDR* of the undoped device is 87.94 dB, while the $Na_{0.07}Cs_{1.93}AgBiBr_6$ device demonstrates an improved *LDR* of 98.75 dB. Combining the linear response shown in Figure 8b,c, the increase in *LDR* indicates that the photodetector maintains a good response over a broader range of light intensities. Therefore, the increased LDR indicates the beneficial impact of sodium ion doping on device performance, leading to the enhancement of multiple performance metrics in the perovskite photodetector. This is crucial for applications that demand high sensitivity and accuracy.

The *PDCR* serves as a key metric for assessing the sensitivity of a photodetector to a specific ultraviolet wavelength and is defined by the following expression:

$$PDCR = \frac{I_p - I_d}{I_d} \tag{4}$$

The *PDCR* of the undoped $Cs_2AgBiBr_6$ at 5 V is 3.34×10^3, whereas that of doped $Na_{0.07}Cs_{1.93}AgBiBr_6$ reaches 7.57×10^4, representing an increase of over 20 times, which demonstrates that doping significantly enhances photodetection performance.

R and *D**, the key parameters of the photodetector, characterize its response and sensitivity [42]. When considering dark current as the primary source of noise, the defining equations for these parameters can be written as Equations (5) and (6):

$$R = \frac{I_p - I_d}{P \cdot A} \tag{5}$$

$$D* = \frac{R\sqrt{A}}{\sqrt{2eI_d}} \tag{6}$$

where e is the elemental charge, P represents the incident light power, and A is the effective illuminated area of the photodetector (0.785 cm^2).

The variation of these parameters with bias voltage for both undoped and doped devices is shown in Figure 9. Under a light intensity of 5 W/m^2, both responsivity and specific detectivity increase with the applied bias voltage. At a bias voltage of 5 V, the responsivity and specific detectivity of the undoped $Cs_2AgBiBr_6$ are relatively low, at 3.28 mA/W and 7.17×10^{10} Jones, respectively, as shown by the blue curve. In contrast, the corresponding parameters for the Na^+-doped $Na_{0.07}Cs_{1.93}AgBiBr_6$ are as high as 16.23 A/W and 2.92×10^{12} Jones. This demonstrates a significant improvement in the photoelectric detection performance after doping. It is noteworthy that the responsivity of $Cs_2AgBiBr_6$ exhibits a pronounced asymmetry between forward and reverse bias. As seen in the I-V curve in Figure 8a, the dark current increases to some extent under reverse bias, leading to a decrease in responsivity. This asymmetry is attributed to the electrode configuration. In contrast, the $Na_{0.07}Cs_{1.93}AgBiBr_6$ film after doping shows a more uniform response under both forward and reverse bias, which is a result of the enhanced carrier mobility due to doping. A similar trend is observed in the specific detectivity shown in Figure 9b.

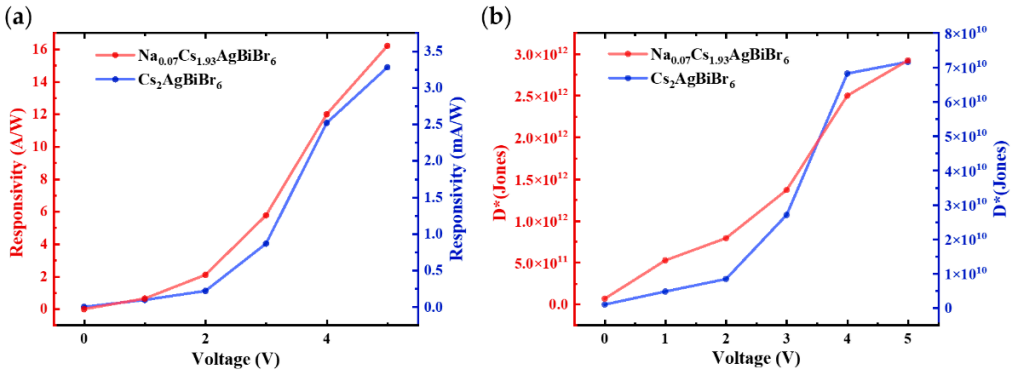


Figure 9. The relationship between (**a**) *R* and (**b**) *D** as a function of bias voltage under 5 W/m^2. The red curves represent $Na_{0.07}Cs_{1.93}AgBiBr_6$, while the blue curves represent $Cs_2AgBiBr_6$.

Additionally, considering the external quantum efficiency (*EQE*) as a parameter to evaluate the intrinsic properties of optoelectronic devices, it is defined as follows:

$$EQE = \frac{hcR}{e\lambda} \tag{7}$$

where h is Planck's constant (6.626×10^{-34} J·S), c is the speed of light, and λ is the wavelength of the incident light, which is 365 nm in this study. Therefore, the *EQE* of the device under a 5 V bias is calculated to be 49.8%.

In Figure 10a,b, the photocurrent response profile reveals that the rise time (τ_r) measured from 10% to 90% of the saturated photocurrent value is 1.613 s, while the decay time (τ_d) measured from 90% to 10% of the saturated value is 1.722 s for $Cs_2AgBiBr_6$. In comparison, the optimized $Na_{0.07}Cs_{1.93}AgBiBr_6$ photodetector demonstrates a significantly reduced rise time of 943 ms and a decay time of 210 ms. The faster response of the $Na_{0.07}Cs_{1.93}AgBiBr_6$ perovskite photodetector highlights its potential as an efficient optical switch for visible light signal detection. This improvement in response speed can be attributed to defect passivation and increased crystallinity of the perovskite film after Na^+ doping, resulting in enhanced overall device performance.

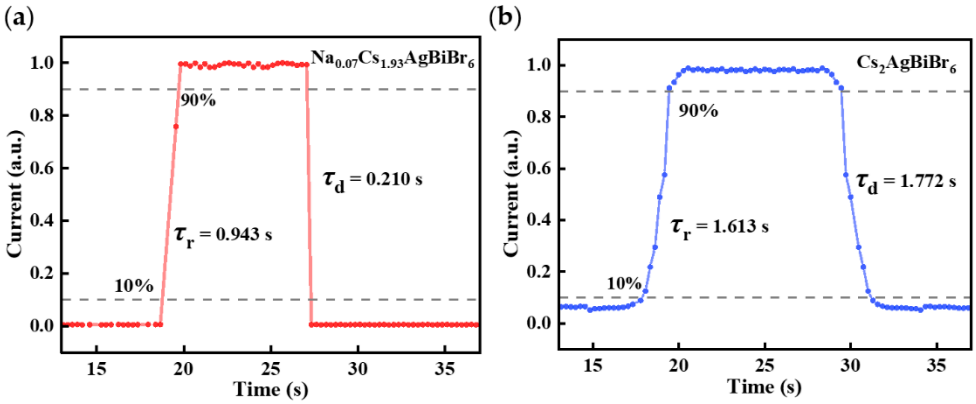


Figure 10. Rise and decay time curves of photocurrent responses of (**a**) $Cs_2AgBiBr_6$ and (**b**) $Na_{0.07}Cs_{1.93}AgBiBr_6$ at 5 V bias under 405 nm alternating illumination with a power of 50 mW.

Figure 11 illustrates the photoconversion mechanism of the $Na_{0.07}Cs_{1.93}AgBiBr_6$ detector under illumination. Upon exposure to 405 nm light, excited-state excitons are generated in $Na_{0.07}Cs_{1.93}AgBiBr_6$. According to the band alignment, electrons tend to move towards the Ag electrode, while holes are transferred to the FTO electrode, thus achieving photoconversion. Compared to the undoped $Cs_2AgBiBr_6$ detector, the $Na_{0.07}Cs_{1.93}AgBiBr_6$ benefits from changes in its bandgap and band alignment, as well as the inherently higher carrier mobility, which leads to a higher responsivity and detectivity in the fabricated photodetector. The doping of Na ions in $Cs_2AgBiBr_6$ effectively enhances optical and electronic properties, demonstrating its potential for improving performance in device applications. This research underscores the promising role of Na^+ doping in optimizing the performance of double perovskite materials for future photodetector technologies.

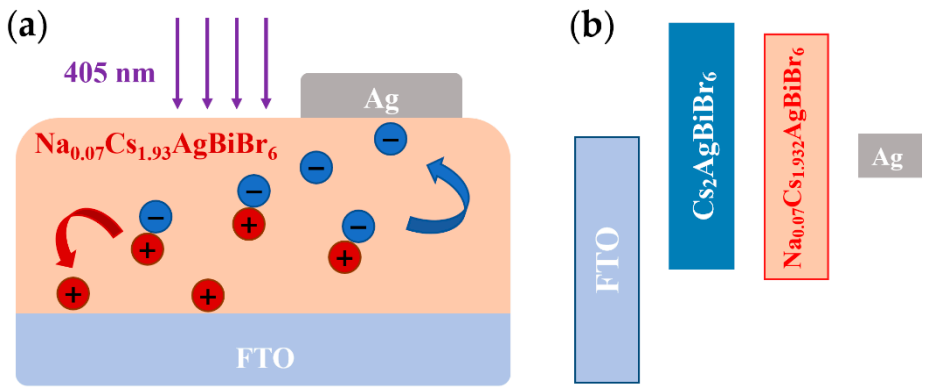


Figure 11. (**a**) Schematic of the charge transfer mechanism in the $Na_{0.07}Cs_{1.93}AgBiBr_6$ detector under illumination. (**b**) Band alignment between $Cs_2AgBiBr_6$, $Na_{0.07}Cs_{1.93}AgBiBr_6$, and the electrodes.

4. Conclusions

In summary, this work successfully synthesized alkali metal ion-doped $Cs_2AgBiBr_6$ perovskite films using a solution-based method and systematically investigated the effects of Na^+ doping on the structural and photoelectric properties of the films. Comprehensive structural analysis revealed that Na^+ doping significantly improved the quality and crystallinity of the films, with minimal impact on the crystal phase structure. At a 3.5% Na^+ doping level, $Na_{0.07}Cs_{1.93}AgBiBr_6$ exhibited an increase in PL intensity by a factor of 2.7 and an enhancement in absorption by a factor of 1.4 compared to undoped $Cs_2AgBiBr_6$. The variable temperature photoluminescence spectra indicate that $Na_{0.07}Cs_{1.93}AgBiBr_6$ exhibits higher exciton binding energy and longitudinal optical phonon energy, demonstrating better thermal stability and weaker nonradiative recombination compared to the undoped $Cs_2AgBiBr_6$. Photodetectors based on $Na_{0.07}Cs_{1.93}AgBiBr_6$ films showed significant improvements compared to the undoped films in low-light dynamic range (*LDR*), photo-to-dark current ratio (*PDCR*), responsivity (*R*), and specific detectivity (*D**), achieving values of 98.75 dB, 7.57×10^4, and 16.23 A/W and 2.92×10^{12} Jones. Furthermore, the $Na_{0.07}Cs_{1.93}AgBiBr_6$-based detectors exhibited a short transient photoresponse and recovery times of 943 ms and 210 ms, making them more suitable for fast-response device applications. This strategy not only provides an effective approach to optimize the structural and photoelectric properties of $Cs_2AgBiBr_6$ films but also offers valuable insights for future material design, demonstrating the potential for developing next-generation high-performance photodetectors.

Supplementary Materials: The following supporting information can be downloaded at: https://www.mdpi.com/article/10.3390/cryst14121068/s1, Figure S1: Refined XRD patterns of $Cs_2AgBiBr_6$ (a) Na-doped and (b) undoped; Table S1: Refined XRD values and original values of $Cs_2AgBiBr_6$; Table S2: Refined XRD values and original values of $Na_{0.05}Cs_{1.95}AgBiBr_6$; Table S3: Refined XRD values and original values of $Na_{0.07}Cs_{1.93}AgBiBr_6$; Table S4: Refined XRD values and original values of $Na_{0.1}Cs_{1.9}AgBiBr_6$.

Author Contributions: Conceptualization, J.D.; methodology, Q.H.; validation, S.S.; formal analysis, Y.W., Y.M., S.S. and A.B.; investigation, Y.W.; resources, C.Z.; data curation, Y.W.; writing—original draft preparation, Y.W.; writing—review and editing, A.B.; visualization, Y.W. and A.B.; supervision, A.B. and J.D.; project administration, A.B. and J.D.; funding acquisition, A.B. All authors have read and agreed to the published version of the manuscript.

Funding: This project was financially supported by the National Natural Science Foundation of China (62305135) and the Postgraduate Research & Practice Innovation Program of Jiangsu Province (KYCX24_4103).

Data Availability Statement: The original contributions presented in the study are included in the article, further inquiries can be directed to the corresponding author.

Conflicts of Interest: The authors declare no conflict of interest.

References

1. Maes, J.; Balcaen, L.; Drijvers, E.; Zhao, Q.; De Roo, J.; Vantomme, A.; Vanhaecke, F.; Geiregat, P.; Hens, Z. Light Absorption Coefficient of $CsPbBr_3$ Perovskite Nanocrystals. *J. Phys. Chem. Lett.* **2018**, *9*, 3093–3097. [CrossRef] [PubMed]
2. Filip, M.R.; Eperon, G.E.; Snaith, H.J.; Giustino, F. Steric engineering of metal-halide perovskites with tunable optical band gaps. *Nat. Commun.* **2014**, *5*, 5757. [CrossRef] [PubMed]
3. Steirer, K.X.; Schulz, P.; Teeter, G.; Stevanovic, V.; Yang, M.; Zhu, K.; Berry, J.J. Defect Tolerance in Methylammonium Lead Triiodide Perovskite. *ACS Energy Lett.* **2016**, *1*, 360–366. [CrossRef]
4. Zhumekenov, A.A.; Saidaminov, M.I.; Haque, M.A.; Alarousu, E.; Sarmah, S.P.; Murali, B.; Dursun, I.; Miao, X.-H.; Abdelhady, A.L.; Wu, T.; et al. Formamidinium Lead Halide Perovskite Crystals with Unprecedented Long Carrier Dynamics and Diffusion Length. *ACS Energy Lett.* **2016**, *1*, 32–37. [CrossRef]
5. Zhang, F.; Lu, H.; Tong, J.; Berry, J.J.; Beard, M.C.; Zhu, K. Advances in two-dimensional organic–inorganic hybrid perovskites. *Energy Environ. Sci.* **2020**, *13*, 1154–1186. [CrossRef]
6. Kim, Y.H.; Cho, H.; Heo, J.H.; Kim, T.S.; Myoung, N.; Lee, C.L.; Im, S.H.; Lee, T.W. Multicolored organic/inorganic hybrid perovskite light-emitting diodes. *Adv. Mater.* **2015**, *27*, 1248–1254. [CrossRef]

7. Ma, S.; Cai, M.; Cheng, T.; Ding, X.; Shi, X.; Alsaedi, A.; Hayat, T.; Ding, Y.; Tan, Z.a.; Dai, S. Two-dimensional organic-inorganic hybrid perovskite: From material properties to device applications. *Sci. China Mater.* **2018**, *61*, 1257–1277. [CrossRef]
8. Wang, F.; Zou, X.; Xu, M.; Wang, H.; Wang, H.; Guo, H.; Guo, J.; Wang, P.; Peng, M.; Wang, Z.; et al. Recent Progress on Electrical and Optical Manipulations of Perovskite Photodetectors. *Adv. Sci.* **2021**, *8*, e2100569. [CrossRef]
9. Wei, H.; Fang, Y.; Mulligan, P.; Chuirazzi, W.; Fang, H.-H.; Wang, C.; Ecker, B.R.; Gao, Y.; Loi, M.A.; Cao, L.; et al. Sensitive X-ray detectors made of methylammonium lead tribromide perovskite single crystals. *Nat. Photonics* **2016**, *10*, 333–339. [CrossRef]
10. Zhang, Q.; Su, R.; Du, W.; Liu, X.; Zhao, L.; Ha, S.T.; Xiong, Q. Advances in Small Perovskite-Based Lasers. *Small Methods* **2017**, *1*, 1700163. [CrossRef]
11. Fang, T.; Wang, T.; Li, X.; Dong, Y.; Bai, S.; Song, J. Perovskite QLED with an external quantum efficiency of over 21% by modulating electronic transport. *Sci. Bull.* **2021**, *66*, 36–43. [CrossRef] [PubMed]
12. Hoye, R.L.Z.; Eyre, L.; Wei, F.; Brivio, F.; Sadhanala, A.; Sun, S.; Li, W.; Zhang, K.H.L.; MacManus-Driscoll, J.L.; Bristowe, P.D.; et al. Fundamental Carrier Lifetime Exceeding 1 µs in $Cs_2AgBiBr_6$ Double Perovskite. *Adv. Mater. Interfaces* **2018**, *5*, 2–9. [CrossRef]
13. Igbari, F.; Wang, R.; Wang, Z.K.; Ma, X.J.; Wang, Q.; Wang, K.L.; Zhang, Y.; Liao, L.S.; Yang, Y. Composition Stoichiometry of $Cs_2AgBiBr_6$ Films for Highly Efficient Lead-Free Perovskite Solar Cells. *Nano Lett.* **2019**, *19*, 2066–2073. [CrossRef] [PubMed]
14. Fang, F.; Li, H.; Fang, S.; Zhou, B.; Huang, F.; Ma, C.; Wan, Y.; Jiang, S.; Wang, Y.; Tian, B.; et al. 2D $Cs_2AgBiBr_6$ with Boosted Light-Matter Interaction for High-Performance Photodetectors. *Adv. Opt. Mater.* **2021**, *9*, 2001930. [CrossRef]
15. Slavney, A.H.; Hu, T.; Lindenberg, A.M.; Karunadasa, H.I. A Bismuth-Halide Double Perovskite with Long Carrier Recombination Lifetime for Photovoltaic Applications. *J. Am. Chem. Soc.* **2016**, *138*, 2138–2141. [CrossRef] [PubMed]
16. Greul, E.; Petrus, M.L.; Binek, A.; Docampo, P.; Bein, T. Highly stable, phase pure $Cs_2AgBiBr_6$ double perovskite thin films for optoelectronic applications. *J. Mater. Chem. A* **2017**, *5*, 19972–19981. [CrossRef]
17. Steele, J.A.; Pan, W.; Martin, C.; Keshavarz, M.; Debroye, E.; Yuan, H.; Banerjee, S.; Fron, E.; Jonckheere, D.; Kim, C.W.; et al. Photophysical Pathways in Highly Sensitive Cs_2 $AgBiBr_6$ Double-Perovskite Single-Crystal X-Ray Detectors. *Adv. Mater.* **2018**, *30*, e1804450. [CrossRef]
18. Yang, J.; Bao, C.; Ning, W.; Wu, B.; Ji, F.; Yan, Z.; Tao, Y.; Liu, J.M.; Sum, T.C.; Bai, S.; et al. Stable, High-Sensitivity and Fast-Response Photodetectors Based on Lead-Free $Cs_2AgBiBr_6$ Double Perovskite Films. *Adv. Opt. Mater.* **2019**, *7*, 1801732. [CrossRef]
19. Zhou, L.; Xu, Y.F.; Chen, B.X.; Kuang, D.B.; Su, C.Y. Synthesis and Photocatalytic Application of Stable Lead-Free Cs_2 $AgBiBr_6$ Perovskite Nanocrystals. *Small* **2018**, *14*, e1703762. [CrossRef]
20. Gao, W.; Ran, C.; Xi, J.; Jiao, B.; Zhang, W.; Wu, M.; Hou, X.; Wu, Z. High-Quality Cs_2 $AgBiBr_6$ Double Perovskite Film for Lead-Free Inverted Planar Heterojunction Solar Cells with 2.2% Efficiency. *Chemphyschem* **2018**, *19*, 1696–1700. [CrossRef]
21. Shuang, Z.; Zhou, H.; Wu, D.; Zhang, X.; Xiao, B.; Ma, G.; Zhang, J.; Wang, H. Low-temperature process for self-powered lead-free Cs2AgBiBr6 perovskite photodetector with high detectivity. *Chem. Eng. J.* **2022**, *433*, 134544. [CrossRef]
22. Biswas, I.; Dey, A.; Dalal, A.; Saha, S.; Nunzi, J.-M.; Mondal, A. Stable, self-biased $Cs_2AgBiBr_6$ thin-film based photodetector by three-step vapor-deposition. *J. Alloys Compd.* **2024**, *976*, 172903. [CrossRef]
23. Rahane, S.N.; Rahane, G.K.; Mandal, A.; Jadhav, Y.; Godha, A.; Rokade, A.; Shah, S.; Hase, Y.; Waghmare, A.; Saykar, N.G.; et al. Lead-Free $Cs_2AgBiCl_6$ Double Perovskite: Experimental and Theoretical Insights into the Self-Trapping for Optoelectronic Applications. *ACS Phys. Chem. Au* **2024**, *4*, 476–489. [CrossRef] [PubMed]
24. Ji, F.; Huang, Y.; Wang, F.; Kobera, L.; Xie, F.; Klarbring, J.; Abbrent, S.; Brus, J.; Yin, C.; Simak, S.I.; et al. Near-Infrared Light-Responsive Cu-Doped $Cs_2AgBiBr_6$. *Adv. Funct. Mater.* **2020**, *30*, 2005521. [CrossRef]
25. Wang, S.; Jiang, W.; Cui, W.; Jiang, W.; Zhao, M.; Sun, J.; Liu, B.; Lai, X.; Shi, K.; Pan, K. Improved Optical Properties of Lead-Free Double Perovskite $Cs_2AgBiBr_6$ Nanocrystals via Na Ions Doping. *Adv. Opt. Mater.* **2023**, *11*, 2202745. [CrossRef]
26. Ding, N.; Shao, L.; Xie, T.; Pan, G.; Zhou, D.; Bai, X.; Lu, S.; Hu, J.; Zhou, J.; Xu, W.; et al. Highly-Sensitive, Stable, and Fast-Response Lead-Free $Cs_2AgBiBr_6$ Double Perovskite Photodetectors Enabled by Synergistic Engineering of Doping Na^+/Ce^{3+} and Integrating Ag Nanoparticles Film. *Laser Photonics Rev.* **2022**, *16*, 2200301. [CrossRef]
27. Chen, Z.; Jiang, X.; Xu, H.; Wang, J.; Zhang, M.; Pan, D.; Jiang, G.; Shahid, M.Z.; Li, Z. Rubidium Doped $Cs_2AgBiBr_6$ Hierarchical Microsphere for Enhanced Photocatalytic CO_2 Reduction. *Small* **2024**, *20*, e2401202. [CrossRef]
28. Chen, H.; Zhang, C.-R.; Liu, Z.-J.; Gong, J.-J.; Zhang, M.-L.; Wu, Y.-Z.; Chen, Y.-H.; Chen, H.-S. Optoelectronic properties of Rb-doped inorganic double perovskite $Cs_2AgBiBr_6$. *Chem. Phys. Lett.* **2021**, *771*, 138501. [CrossRef]
29. Zhang, Z.; Liu, G.; Guo, W.; Li, X.; Zhang, Y.; Wu, C.; Qu, B.; Shi, J.-j.; Chen, Z.; Xiao, L. Black single crystals of lead-free perovskite $Cs_2Ag(Bi:Ru)Br_6$ with an intermediate band. *Mater. Adv.* **2022**, *3*, 4932–4937. [CrossRef]
30. Cen, G.; Sheng, H.; Wang, Z.; Yi, L.; Sun, H.; An, Y.; Zhao, C.; Mai, W. Boosting photodetection performance of $Cs_2AgBiBr_6$ through A-site Rb substitution and interfacial engineering. *J. Colloid Interface Sci.* **2023**, *652*, 34–40. [CrossRef]
31. Yan, G.; Jiang, B.; Xiao, Y.; Zhao, C.; Yuan, Y.; Liang, Z. Alkali metal ions induced high-quality all-inorganic $Cs_2AgBiBr_6$ perovskite films for flexible self-powered photodetectors. *Appl. Surf. Sci.* **2022**, *579*, 152198. [CrossRef]
32. Zhang, Z.; Wu, C.; Wang, D.; Liu, G.; Zhang, Q.; Luo, W.; Qi, X.; Guo, X.; Zhang, Y.; Lao, Y.; et al. Improvement of $Cs_2AgBiBr_6$ double perovskite solar cell by rubidium doping. *Org. Electron.* **2019**, *74*, 204–210. [CrossRef]
33. Wu, C.; Zhang, Q.; Liu, Y.; Luo, W.; Guo, X.; Huang, Z.; Ting, H.; Sun, W.; Zhong, X.; Wei, S.; et al. The Dawn of Lead-Free Perovskite Solar Cell: Highly Stable Double Perovskite $Cs_2AgBiBr_6$ Film. *Adv. Sci.* **2018**, *5*, 1700759. [CrossRef] [PubMed]
34. Wu, R.; Wang, Q.; Yang, S.; Wu, L.; Gong, S.; Han, Q.; Wu, W. Enhanced thermal stability of exciton recombination in $CsPbI_3$ perovskite nanocrystals via zinc alloying. *J. Alloys Compd.* **2021**, *857*, 157574. [CrossRef]

35. Gebhardt, J.; Elsässer, C. The Electronic Structure of $Cs_2AgBiBr_6$ at Room Temperature. *Phys. Status Solidi (b)* **2022**, *259*, 2200124. [CrossRef]
36. Lei, H.; Hardy, D.; Gao, F. Lead-Free Double Perovskite $Cs_2AgBiBr_6$: Fundamentals, Applications, and Perspectives. *Adv. Funct. Mater.* **2021**, *31*, 2105898. [CrossRef]
37. Bekenstein, Y.; Dahl, J.C.; Huang, J.; Osowiecki, W.T.; Swabeck, J.K.; Chan, E.M.; Yang, P.; Alivisatos, A.P. The Making and Breaking of Lead-Free Double Perovskite Nanocrystals of Cesium Silver-Bismuth Halide Compositions. *Nano Lett.* **2018**, *18*, 3502–3508. [CrossRef]
38. Yao, M.M.; Wang, L.; Yao, J.S.; Wang, K.H.; Chen, C.; Zhu, B.S.; Yang, J.N.; Wang, J.J.; Xu, W.P.; Zhang, Q.; et al. Improving Lead-Free Double Perovskite Cs2NaBiCl6 Nanocrystal Optical Properties via Ion Doping. *Adv. Opt. Mater.* **2020**, *8*, 1901919. [CrossRef]
39. Wright, A.D.; Buizza, L.R.V.; Savill, K.J.; Longo, G.; Snaith, H.J.; Johnston, M.B.; Herz, L.M. Ultrafast Excited-State Localization in $Cs_2AgBiBr_6$ Double Perovskite. *J. Phys. Chem. Lett.* **2021**, *12*, 3352–3360. [CrossRef]
40. Shi, Z.; Li, Y.; Zhang, Y.; Chen, Y.; Li, X.; Wu, D.; Xu, T.; Shan, C.; Du, G. High-Efficiency and Air-Stable Perovskite Quantum Dots Light-Emitting Diodes with an All-Inorganic Heterostructure. *Nano Lett.* **2017**, *17*, 313–321. [CrossRef]
41. Sun, S.; Yuan, D.; Xu, Y.; Wang, A.; Deng, Z. Ligand-Mediated Synthesis of Shape-Controlled Cesium Lead Halide Perovskite Nanocrystals via Reprecipitation Process at Room Temperature. *ACS Nano* **2016**, *10*, 3648–3657. [CrossRef] [PubMed]
42. Sze, S.M.; Ng, K.K. *Physics of Semiconductor Devices*; John Wiley & Sons: Hoboken, NJ, USA, 2021.

Disclaimer/Publisher's Note: The statements, opinions and data contained in all publications are solely those of the individual author(s) and contributor(s) and not of MDPI and/or the editor(s). MDPI and/or the editor(s) disclaim responsibility for any injury to people or property resulting from any ideas, methods, instructions or products referred to in the content.